

Water Quality Seasonal Variability (2000 to 2015) in Yangtze River Estuary and Its Adjacent Coastal Area

Xianping Yang, Leonid Sokoletsky* and Hui Wu

State Key Laboratory of Estuarine and Coastal Research, East China Normal University, Shanghai, China

*Corresponding author: Leonid Sokoletsky, State Key Laboratory of Estuarine and Coastal Research, East China Normal University, Shanghai, China, Tel: 086-021-52134943; E-mail: sokoletsky.leonid@gmail.com

Rec date: September 22, 2017; Acc date: October 26, 2017; Pub date: October 30, 2017

Copyright: © 2017 Yang X, et al. This is an open-access article distributed under the terms of the Creative Commons Attribution License, which permits unrestricted use, distribution, and reproduction in any medium, provided the original author and source are credited.

Abstract

Three separate algorithms: 1) Modified NIR-SWIR atmospheric correction, 2) Suspended sediment concentration (SSC), and 3) Diffuse attenuation coefficient at 490 nm, $K_d(490)$ were developed and used for mapping SSC and $K_d(490)$ for the East China natural waters. A geographic area located between 27-35°N and 119-125°E was selected to analyze wet (flood) and dry seasons from 2000 to 2015. Remote sensing acquisition has been realized using the MODIS/Terra and MODIS/Aqua satellite sensors. Results showed large differences between these seasons in terms of spatial pattern of SSC and $K_d(490)$ levels: SSC and $K_d(490)$ values were higher during the dry season than during the flood season in the most part of area for most of the area. The area with high SSC > 80 gm⁻³ [or, correspondingly, $K_d(490)$ > 2.3 m⁻¹] within the Subei Bank of the Yellow Sea and the Zhejiang coastal area was estimated to be almost twice as large during the dry season when compared to the wet season. Results also revealed an impact of the Three Gorges Dam power station on the water quality in the Yangtze River Estuary.

Keywords: Turbid estuarine and coastal waters; Atmospheric correction; Remote-sensing reflectance; Suspended sediment concentration; Diffuse attenuation coefficient

Introduction

An increasing population and the accompanied rising anthropogenic pressure in the East China coastal region, comprising the Yangtze River Estuary (YRE) and its adjacent coastal area (ACA), dictate the necessity for improved management and monitoring of these waters. From optical point of view, the part of ACA far away from the coastal line (open oceanic waters) may be referred to the Case 1 waters, i.e., such waters for which phytoplankton and their immediate detrital material, along with the water itself, do control the optical properties of the medium [1-3]. Oppositely, the YRE and the nearest part of ACA, for which the suspended sediment concentration (SSC) is the central factor influencing the optical properties, are the typical Case 2 waters [1-3].

Thus, SSC, one of the most important water quality components, especially in inland, estuarine, and coastal turbid areas [4-6], directly affects optical properties such as color, light transmittance, absorption, backscattering, scattering angular distribution, and reflectance [7-9], and it is strongly responsible for the abundance and the transport of carbon, phytoplankton, nutrients, metals, and pollutants in aquatic environments [10-12].

In sediment-dominated Case 2 waters, the SSC is closely related with the diffuse attenuation coefficient (K_d), which in turn has been used for different systems of water quality classification [13-20] and also in models of light penetration, for example, to compute a primary production as a function of light available at depth [21-23]. It is important that K_d is one of the geophysical parameters that can be derived from ocean color images [24-26]. K_d together with SSC, are important water quality parameters (WQPs), and they were the focus

of many *in situ* measurements and remote sensing investigations performed in East China inland, estuarine and coastal waters [19,20,26-46].

In many of these publications, the seasonal variations in SSC and $K_d(\lambda)$ were noted during both field [27,28,32,33,35,38,41-43,45,46] and remote-sensing [26,32-34,36,38,40-47] observations. These publications give a somewhat contradictory picture of the seasonal variations of SSC and $K_d(490)$ in East China waters. For example, Shi and Wang [26], based on results obtained during 2002-2008 from the Moderate Resolution Imaging Spectroradiometer (MODIS) onboard the satellite Aqua, concluded that $K_d(490)$ values derived for Subei Bank (SB) of the Yellow Sea, Taihu Lake (TL), and Hangzhou Bay (HB) were substantially larger in winter than in summer, while for YRE the averaged (within the 2002-2008) seasonal values of $K_d(\lambda)$ were approximately the same for all seasons.

However, He et al. [39] wrote, "Numerous factors can affect temporal variations of the TSM in HZB ('total suspended matter in Hangzhou Bay'-our comm.). In general, the TSM concentrations inputted by the Changjiang and Qiantang Rivers are much higher in the wet season with large discharge from May through October, than in the dry season with low discharge from November through April [28,37].

Oppositely, results found by Ref. [26-28,33,35,36,38,39,42] show that generally SSC and $K_d(490)$ in YRE, HB, SB, and TL are significantly higher in the dry season than in the wet (flood) season. Moreover, from Ref. [26,36,38] follows even more detailed rule for all four seasonal average values of SSC and $K_d(490)$, which may be written, in short form, as: {Summer} < {Autumn} < {Spring} < {Winter}.

This obvious contradiction between the above statement in Ref. [39] and the conclusions from the other publications (and from Ref. [39] itself) could be caused by the separate deviations from the general picture, observed in the two stations in the inner part of YRE by Chen

et al. [28] and at the Nanjing station (Lower Yangtze River) by Mao et al. [47]. This is in accordance with conclusions made by Chen [27] that "in the inner estuary predominantly affected by river water discharge, the SSC is higher during the summer than during the winter. However, the SSC out the mouth of Yangtze Estuary is higher during the winter than during the summer, hence the sediment discharge carried by the runoff does not directly affect the SSC of the study area."

Another important task is a monitoring of the multi-year SSC and $K_d(490)$ dynamics, strongly related with activity of the Three Gorges Dam (TGD), the world's largest power station, spanning the Yangtze River [32,35,48]. Three main periods may be highlighted for the purposes of the current study: before 2006 (when the dam body was completed), after 2012 (when the dam project was completed and become fully functional) and between 2006 and 2012 (transition period).

Therefore, our aim is to study the seasonal and multi-year water quality dynamics for East China natural waters based on the last achievements in atmospheric and ocean optics. With this purpose, we have performed remote sensing observations of SSC and $K_d(490)$ via MODIS, which is onboard two NASA spacecrafts (Terra and Aqua). We have used images obtained by this satellite sensor (with a spatial resolution of 1 km) over the East China area, during 2000-2015 and grouped all images for flood (May to October) and dry (November to the next April) seasons. This allowed us to check, extend, and improve current knowledge of water quality in this region. Thus, these new results span much longer time period and simultaneously they better seasonally grouped than it was in previous studies of the area.

Geographical region and observations

The coastal region along the YRE and ACA (Figure 1) is one of the most active economic belts, and it is impacted by huge stresses from anthropogenic activities and population growth. The Yangtze River is the longest river (6300 km) in Asia, carrying abundant sediment (470 Mt/yr averagely) to its estuary [48].

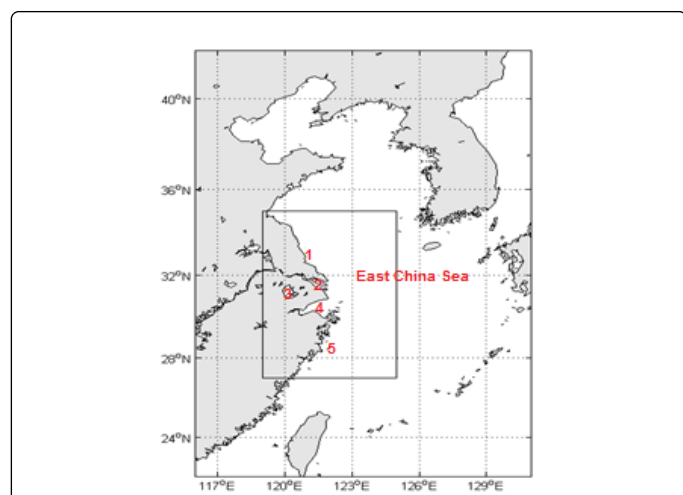


Figure 1: Map of the eastern Chinese waters. Numbers 1-5 correspond to Subei Bank of the Yellow Sea, Yangtze River Estuary, Taihu Lake, Hangzhou Bay, and Zhejiang coastal area, respectively.

The appropriate literature shows that the SSC varies from 1~70 gm^{-3} in East China Sea (ECS), up to ~150 gm^{-3} in Taihu Lake, up to ~2000 gm^{-3} in YRE, up to ~2500 gm^{-3} in the Subei Bank of the Yellow Sea, and up to ~8000 gm^{-3} in the HB [30,31,33,35,36,38,39,42-46]. These values indicate that the suspended sediment ranges in the YRE and its ACA differ from most worldwide estuaries and coastal zones. Similarly, the $K_d(490)$ values found in the literature [26,34,36,37] demonstrate huge variability in this parameter, which strongly exceeded the limits (0.02-1.1 m^{-1}) provided by the classical Jerlov's classification for $K_d(490)$ [13].

Three databases were used in the present work for model development and validation purposes: 1) SSC and laboratory tank radiometric measurements performed in July 2006 (118 samples), when sediment samples used in tank experiments were collected in the Yangtze River and Yellow River estuaries [31]; 2) *In situ* measurements of SSC, radiometry, and inherent optical properties (IOPs), including absorption a , attenuation c , and back scattering b_b coefficients, performed on May 4-12, 2011, in the YRE and its ACA (19 samples); and 3) *in situ* measurements of the chlorophyll concentration (Chl), SSC, and IOPs, including a , c , b_b , and colored dissolved organic matter (CDOM) absorption, performed on February 21-March 10, 2014, in the YRE and its ACA (94 samples) [46].

The images of MODIS/Terra from March 2000 to December 2015 were downloaded from the Level 1 Atmosphere Archive and Distribution System (LAADS), <https://ladsweb.nascom.nasa.gov/>. MODIS/Aqua images from January 2010 to December 2015 were also downloaded from the LAADS system as a supplement. In total, 908 MODIS/Terra images and 192 MODIS/Aqua images were processed during the 16-year time period.

Development of a New (Modified NIR-SWIR) Atmospheric Correction Approach

Introduction to a new approach

Aerosol type and load can be observed by ground stations, however, generally there is a problem with the simultaneous collection of aerosol data and satellite images, especially for the sea and ocean where there are no meteorological stations. Nevertheless, numerous atmospheric correction approaches were developed during last decades. Atmospheric and ocean optics pioneers, such as Howard Gordon, assumed that the ocean is totally absorbing in the band centered at $\lambda=750$ nm, i.e., $L_w(750)=0$ [49]. Moreover, worldwide *in situ* observations [50] have shown that in very clear waters with the pigment concentration $C<0.25$ mg m^{-3} , even $L_w(\lambda \geq 670$ nm) can be assumed to be zero. Similar assumptions were widely used in numerous studies (e.g., [51-53]). The further development of such approach was suggested by Wang and Shi (2005) [54], who assumed that the ocean is black (i.e., $b_b(\lambda)=L_w(\lambda)=R_{rs}(\lambda)=0$) at the short-wave infrared (SWIR) band to solve an atmospheric correction problem for the turbid Case 2 natural waters.

On the other hand, another strategy, so called "the best fit," is popular, and it is commonly used for the remote sensing retrieval of aerosol properties for land [55,56] and ocean [57,58]. Lookup tables (LUTs) generating preliminary, are used for comparison of the measured water-leaving radiance with the LUTs values for determination of aerosol types or/and other atmospheric parameters. The spectral remote-sensing reflectance R_{rs} (or normalized water-

leaving radiance, L_{wn}) values derived from LUTs then may be used as inputs for SSC and K_d products.

Some serious problems may be noted, however, under exploration of the LUTs: 1) Not all LUTs are achievable for customary researchers; 2) A lot of satellite images do not have SWIR bands, which are used often by LUTs; and 3) Our experience shows that results derived from the NIR-SWIR based on the using LUTs are not reasonable enough.

Therefore, we suggest the compromise variant of the atmospheric correction algorithm by combining the “best fit” and NIR-SWIR approaches as follows:

- For Case 1 waters, the black ocean assumption is accepted for all NIR and SWIR bands, while for Case 2 waters, it is only accepted for SWIR bands.
- A boundary between Case 1 and Case 2 waters has been determined by the turbid water index, $T_{ind}(\lambda_i, \lambda_j)$, which may be expressed approximately [59,60] [under condition that the water-leaving reflectance $\rho_w(\lambda_j) \ll \rho_w(\lambda_i)$] as $T_{ind}(\lambda_i, \lambda_j) \approx 1 + \rho_w, TOA(\lambda_i) / \rho_a(\lambda_i) = 1 + L_w, TOA(\lambda_i) / L_a(\lambda_i)$ where index “TOA” means top-of-atmosphere level; we accepted $T_{ind}(746.4, 1241.6) = 1.3$ (here 746.4 and 1241.6 nm are the central wavelengths of 15th and 5th MODIS bands, respectively) as a boundary value following Ref. [59,60].
- For MODIS-derived images with NIR and SWIR bands, the NIR-SWIR atmospheric correction was applied.

- For satellite images without SWIR band, the NIR bands were exploited first for the Case 1 waters, and then the same aerosol type as was derived for these waters was applied to the Case 2 waters as well.

Another problem with the NIR-SWIR atmospheric correction that not all satellite sensors have SWIR bands. The Geostationary Ocean Color Imager (GOCI) launched on June 2010 by South Korea [39,43] is an example of such sensor. The sensor has a spatial resolution of 500 m, temporal resolution of 1 hour, and two NIR bands centered about 745 and 865 nm, but does not has SWIR bands. Thus, we suggest to use these two bands for an atmospheric correction in Case 1 waters (i.e., for ACA), and then to do atmospheric correction for the remaining Case 2 waters with preliminary derived (from LUTs) aerosol type.

Generation of LUTs

A preliminary lookup table was generated for four small modes (“S”) and five large modes (“L”) [56,58] of aerosols shown in Table 1, assuming bimodal lognormal aerosol size distribution (ASD) [56]. Details of such ASD may be found in Ref. [56]. Table 1 contains a full set of the complex refractive indices and ASD parameters for all nine aerosols modes included in this LUT.

Mode	Refractive indices				ASD parameters (nm)			Aerosol type
	$\lambda=470-860$ nm	$\lambda=1240$ nm	$\lambda=1640$ nm	$\lambda=2130$ nm	r_g	σ_r	r_{ef}	
S1	1.45-0.0035i	1.45-0.0035i	1.43-0.01i	1.40-0.005i	0.07	0.4	0.1	WWS
S2	1.45-0.0035i	1.45-0.0035i	1.43-0.01i	1.40-0.005i	0.06	0.6	0.15	WWS
S3	1.40-0.002i	1.40-0.002i	1.39-0.005i	1.36-0.003i	0.08	0.6	0.2	WSWH
S4	1.40-0.002i	1.40-0.002i	1.39-0.005i	1.36-0.003i	0.1	0.6	0.25	WSWH
L1	1.45-0.0035i	1.45-0.0035i	1.43-0.0035i	1.43-0.0035i	0.4	0.6	0.98	WSS
L2	1.45-0.0035i	1.45-0.0035i	1.43-0.0035i	1.43-0.0035i	0.6	0.6	1.48	WSS
L3	1.45-0.0035i	1.45-0.0035i	1.43-0.0035i	1.43-0.0035i	0.8	0.6	1.98	WSS
L4	1.53-0.003i (470) 1.53-0.001i (550) 1.53-0.000i (660) 1.53-0.000i (860)	1.46-0.000i	1.46-0.000i	1.46-0.000i	0.6	0.6	1.48	DL
L5	1.53-0.003i (470) 1.53-0.001i (550) 1.53-0.000i (660) 1.53-0.000i (860)	1.46-0.000i	1.46-0.000i	1.46-0.000i	0.5	0.8	2.5	DL

Table 1: Complex refractive indices, geometric mean radii (r_g), standard deviations of radii (σ_r) and effective radii (r_{ef}) for small (S₁ to S₄) and large modes (L₁ to L₅) used in the MODIS LUT. ASD (aerosol size distribution); WSWH (water soluble with humidity), WWS (wet water soluble), WSS (wet sea salt), DL (dust-like).

The output [$R_{rs}(\lambda)$] LUT was calculated by using 6S code with different values of aerosol total loading expressed through the aerosol optical thickness τ_a at 550 nm. We have used five different values of τ_a (550) for calculations: 0 (a pure molecular atmosphere), 2 (a very turbid atmosphere observed, for example, during dust or biomass

burning events [61-63]), and three intermediate values: 0.2, 0.5, and 1.0. Thus, the final LUT contains $9 \times 5 = 45$ rows (it is not shown here).

Validation of the Atmospheric Correction Algorithm

Standard (MOD09) and modified NIR-SWIR algorithms vs. *in situ* values

The data obtained from the extensive field campaigns along YRE and its ACA were used for validation of the atmospheric correction algorithm. Details for the field and satellite pixels, which were found appropriate for validation purposes (due to their spatial and temporal closeness), are given in Table 2.

Fig ID	St. ID	Date	Site	Water Type	Time (UTC)	Lat (deg N)	Long (deg E)
a	A7-1	3/9/2014	HB	Case 2	6:18	30.640	122.249
					5:05	30.636	122.249
b	B7	2/21/2014	YRE	Case 2	5:47	31.327	122.305
					5:05	31.326	122.302
c	D2	5/7/2011	YRE	Case 2	5:01	30.995	122.250
					5:35	31.001	122.253
d	D1	5/7/2011	YRE	Case 2	7:00	30.999	122.041
					5:35	30.996	122.036

Table 2: Match-up stations selected for validation of the modified NIR-SWIR algorithm. All UTC times referred to are morning hours. Times (UTC) and geographical coordinates belonging to each station are shown for *in situ* and remote sensing observations in the upper and bottom rows, respectively.

This table demonstrate that the maximal temporal difference between corresponding pixels does not exceed 1.4 hours, and distances between them are shorter than 700 m. Below (Figure 2), we show examples of the spectral $R_{rs}(\lambda)$ obtained from the field observations and satellite monitoring in the area. In addition to our (modified NIR-SWIR algorithm), we show here the results derived from the standard MOD09 atmospheric correction algorithm, created by the MODIS Land Surface Reflectance Science Computing Facility [65,66]. The output spectral surface reflectance $\rho_s(\lambda)$ for this algorithm may be presented with good accuracy (assuming the upwelling light as completely diffuse and unpolarized) as $\rho_s(\lambda) = \pi R_{rs}(\lambda)$ [13,20,67,68].

The results undoubtedly confirm a significant contribution of water-leaving radiance into the sensor level signal for the NIR bands [20,29-34,36-39,41-44,46,54,60]. They also show that the modified NIR-SWIR atmospheric correction algorithm performed generally better than the standard MOD09 algorithm for the highly variable waters under consideration. Besides, it is obvious that there is a closeness between measured *in situ* and predicted from the satellite imagery values of $R_{rs}(\lambda)$, especially in the green-NIR spectral range. However, at $\lambda < 550$ nm, the modified NIR-SWIR approach may slightly underestimate (Figure 2a-2c) or overestimate (Figure 2d) *in situ* $R_{rs}(\lambda)$ values.

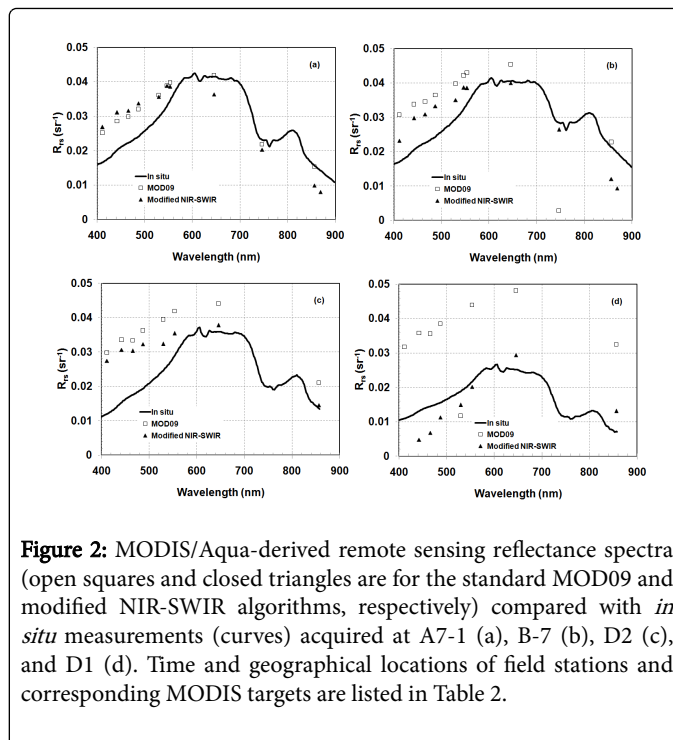


Figure 2: MODIS/Aqua-derived remote sensing reflectance spectra (open squares and closed triangles are for the standard MOD09 and modified NIR-SWIR algorithms, respectively) compared with *in situ* measurements (curves) acquired at A7-1 (a), B-7 (b), D2 (c), and D1 (d). Time and geographical locations of field stations and corresponding MODIS targets are listed in Table 2.

Nevertheless, as numerous studies show (see, e.g., reviews in Ref. [46,64]), wavelengths $\lambda > 550$ nm (where not strong impact of chlorophyll and dissolved organic matter absorption) should be used for SSC and $K_d(490)$ retrievals in turbid waters. Moreover, our previous search of the best MODIS bands for SSC retrieval led to using the fourth band centered at 553.6 nm and the first band centered at 645.5 nm, for *in situ* [64] and remote sensing [46] algorithms.

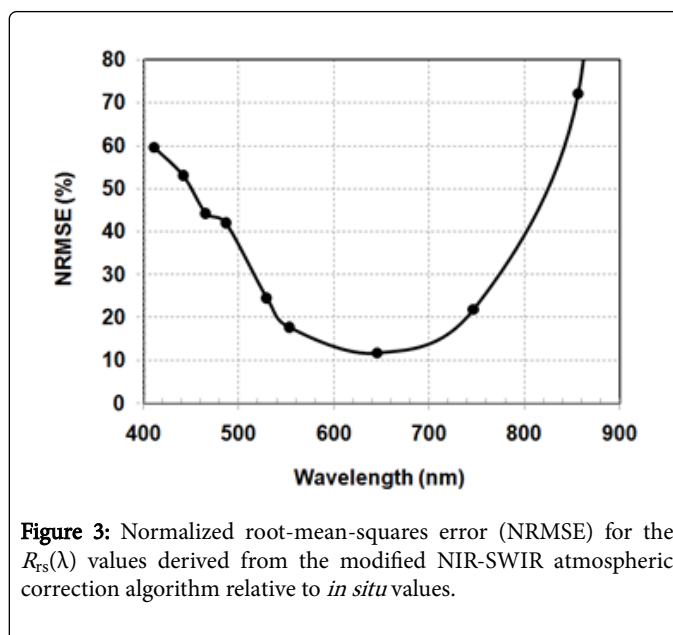


Figure 3: Normalized root-mean-squares error (NRMSE) for the $R_{rs}(\lambda)$ values derived from the modified NIR-SWIR atmospheric correction algorithm relative to *in situ* values.

At present, we have found that these two wavelengths yield the minimum of the normalized (to the mean measured *in situ* values) root-mean-squares error (NRMSE) for the remote sensing $R_{rs}(\lambda)$

values relative to *in situ* values; NRMSE=17.7% and 11.7%, respectively (Figure 3), which confirms our previous choice of these wavelengths.

Modified NIR-SWIR vs. standard (MOD09) algorithm

Figure 4 demonstrates comparison results between the modified NIR-SWIR and MOD09 algorithms for April 5, 2011. It is obvious that both approaches yield close results for the turbid waters, with $R_{rs}(645.5)$ approximately more than 0.02 sr^{-1} [that corresponds to $\text{SSC} > 24 \text{ gm}^{-3}$, $R_{rs}(553.6) > 0.026 \text{ sr}^{-1}$, $R_{rs}(645.5)/R_{rs}(553.6) > 0.76$, and $K_d(0^\circ, 490) > 0.70 \text{ m}^{-1}$, according to our algorithm]; however, there are sometimes large discrepancies for the more clear waters.

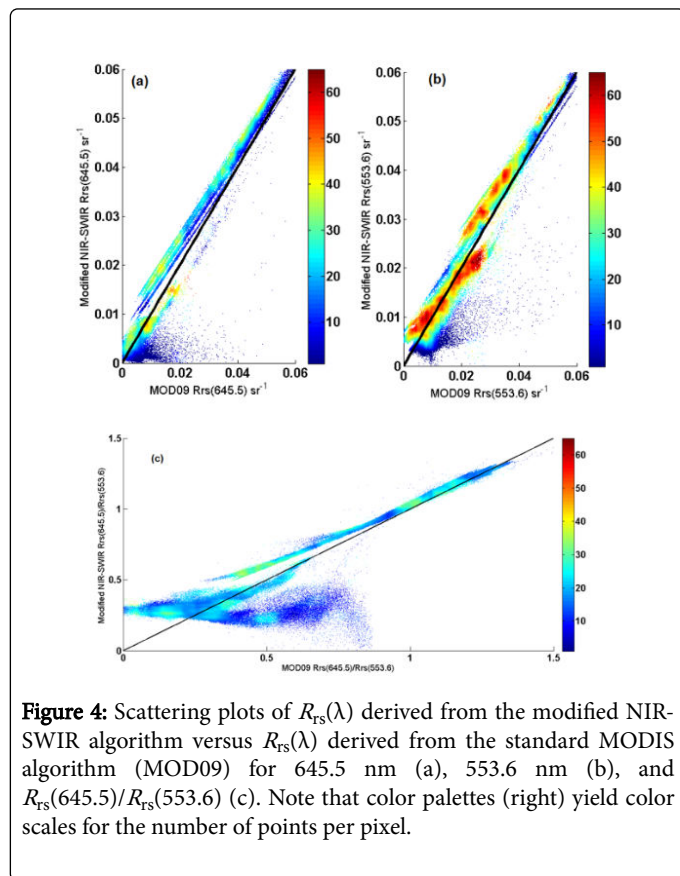


Figure 4: Scattering plots of $R_{rs}(\lambda)$ derived from the modified NIR-SWIR algorithm versus $R_{rs}(\lambda)$ derived from the standard MODIS algorithm (MOD09) for 645.5 nm (a), 553.6 nm (b), and $R_{rs}(645.5)/R_{rs}(553.6)$ (c). Note that color palettes (right) yield color scales for the number of points per pixel.

Cloud Mask

Empirical cloud masking was based on testing two quantities: the atmospheric-corrected $R_{rs}(\lambda)$ at the bands centered at 856.6 nm and 1241.6 nm (the second and fifth MODIS bands, respectively). The pixel under investigation has considered as a cloud pixel, when $R_{rs}(856.6) > 0.08$ or $R_{rs}(1241.6) > 0.006$.

SSC Retrieval

Retrieval of SSC (in gm^{-3}) for the subsurface layer (accepted as the layer lying between 0- and 1 m below the air-sea surface) was realized by the model suggested by [46,64] as follows:

$$\text{SSC} = \begin{cases} 1 \text{ gm}^{-3}, & \text{if } R_{rs}(645.5) < 0 \text{ else} \\ \exp(8X - 7X^2 + X^3 + 2X^4 + 0.1X^5) \end{cases} \quad (1)$$

where $X = R_{rs}(645.5)/R_{rs}(553.6)$.

$K_d(0^\circ, 490 \text{ nm})$ Retrieval

An estimation of diffuse attenuation coefficient at zenith angle (i.e., at solar zenith angle $\theta_0 = 0^\circ$) and near surface (layer < 1 m) was performed as follows:

$K_d(0^\circ, 490) = 0.03012(\text{SSC})^{0.9895}$ (2) Eq. (2) was derived from our three databases and following Gordon's (quasi-single-scattering) approximation, QSSA [69,70]: $K_d(0^\circ, 490) = a(490) + b_b(490)$ (3) It was shown in Ref. [71] that QSSA yields very accurate solutions for the near surface layers of natural waters with widely varied optical conditions.

Results and Discussion

Remote-sensing seasonal analysis of water quality parameters was performed for the East China geographical area during 2000-2015 (Figure 5) based on the sub-algorithms described above, namely, the modified NIR-SWIR atmospheric correction (with cloud masking), SSC, and $K_d(0^\circ, 490)$. We proceeded with all achievable (mostly cloud free) images for this time period and averaged results for each year and for two seasons: the flood (May to October) and the dry (November to the next April) seasons, according to [27,28,35,40,47]. All images were decomposed into $0.05^\circ \times 0.05^\circ$ boxes in the 27°N - 35°N and 119°E - 125°E geographical area.

Our results actually correspond to numerous *in situ* and remote observations [26-28,33,36,38,39,42], that reported seasonal features in the region, namely, generally higher values of SSC and $K_d(0^\circ, 490)$ during the dry season when compared to the wet season. However, this seasonal feature may be different for different years and sub-areas. The most obvious and multi-year stable situation was observed in the East China Sea, Subei Bank, Taihu Lake, Hangzhou Bay, and Zhejiang coastal area. For example, in the ECS a multi-year water transparency is the rather high, with $\text{SSC} < 20 \text{ gm}^{-3}$ (that corresponds the Jerlov 7C water type with $K_d(0^\circ, 490) < 0.58 \text{ m}^{-1}$; see algorithm above and Ref. [13,72] for details) regardless of the year or season of the year. However, four other areas -SB, TL, HB, and ZCA-have shown clear seasonal features during the whole time period (2000-2015).

The most variable multi-year results were found in the South Branch of YRE, namely, very high SSC values ($\sim 1000 \text{ gm}^{-3}$ and more) observed there in 2000, 2001, 2003, 2006, and 2007 flood seasons; however, it was not the case in 2008-2015. Obviously, the YRE accepted a substantial amount of sediments originating from the freshwater discharge-carried sediments of the Yangtze River before 2008. In these years, SSC and $K_d(0^\circ, 490)$ stayed approximately the same during the whole year, i.e., without significant seasonal differences. It is worth to note that such situation may be explained by different balancing factors, namely, large concentrations of suspended matter discharged by Yangtze River during wet seasons, from one side and stronger wind wave and weaker thermal stratification in winter seasons, from another side.

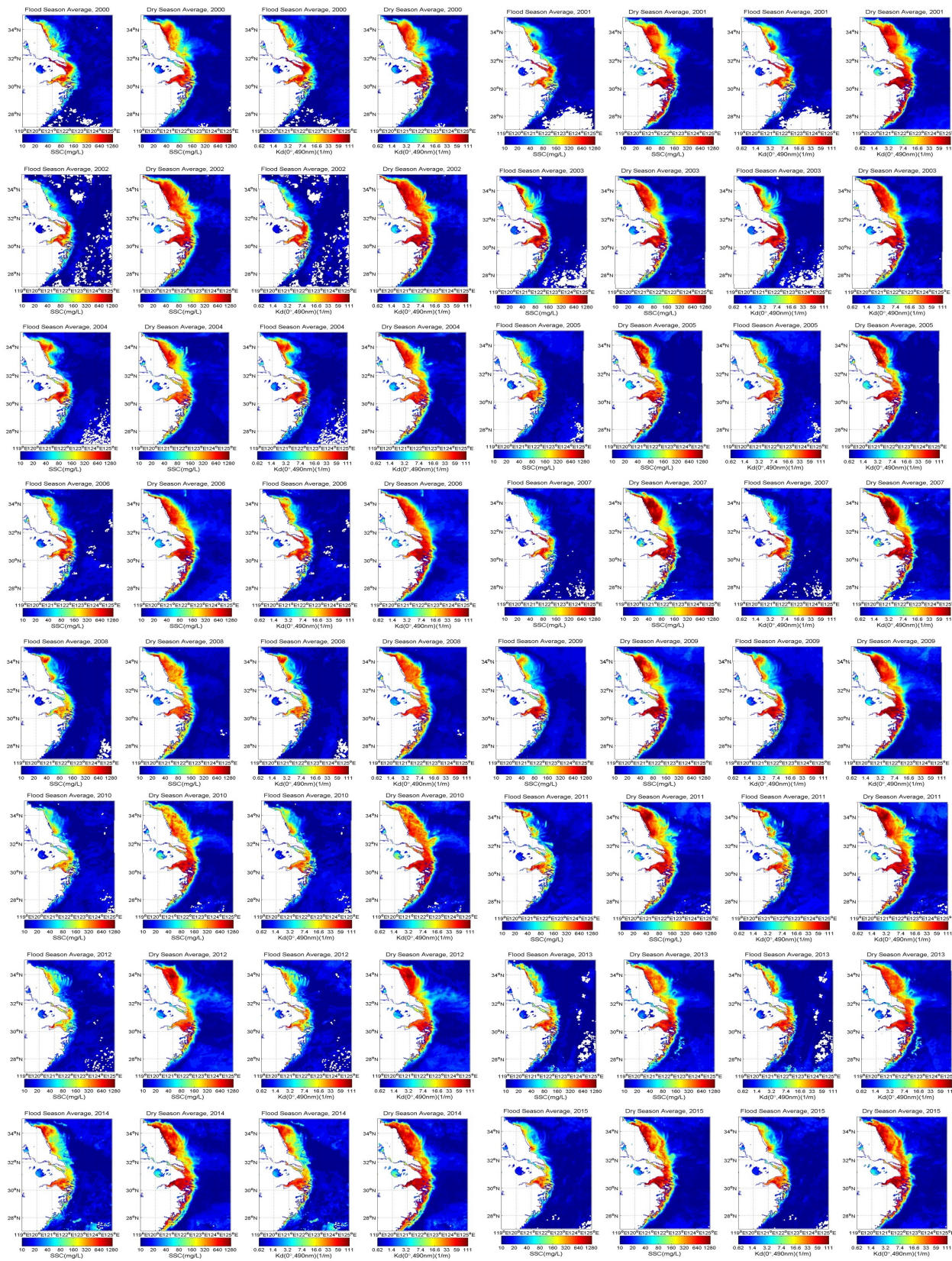


Figure 5: The flood season and dry season average of SSC and K_d (0° , 490 nm) derived from 2000 to 2015 MODIS images.

After completion in 2006 of the TGD, significant amounts of sediments that used to be flushed away were captured by the dam, decreasing sediment load and SSC downstream of the river and the YRE [32,35,48]. Moreover, a field study by Li et al. [35] has shown that the most dramatic decline of sediment discharge in the Lower Yangtze River (at Datong) -more than twice comparing 2003-2009 vs. 1950-2002- happened from April to November, i.e., mostly in the flood season. Our results (Figure 5) completely confirm these field observations, showing significant decrease of SSC in the Lower Yangtze River since 2008, during the flood months. Interesting to note that this dramatic decline of sediment discharge occurs on the background of relatively weak decline (less than 20%) of water discharge in the Lower Yangtze River during the wet season (see Figure 2 in Ref. [35]).

For numerical presentation of results, we have calculated total turbid area for YRE and ACA with $SSC > 80 \text{ gm}^{-3}$ [this corresponds $K_d(0^{\circ}, 490) > 2.3 \text{ m}^{-1}$ according to our optical model] for each false color image and then summarized results for each year in Table 3 and Figure 6.

Year	Flood season area (km ²)	Dry season area (km ²)
2000	40400	59900
2001	35300	75600
2002	29700	81600
2003	45700	66800
2004	37000	64000
2005	36900	59400
2006	39500	70400
2007	24500	70500
2008	32300	67100
2009	36000	68400
2010	30900	73100
2011	34700	79500
2012	28100	59400
2013	40800	68000
2014	51500	79600
2015	31600	72000

Table 3: The flood and dry seasonal areas in with $SSC > 80 \text{ gm}^{-3}$.

These numerical results confirm a general trend observed in the East China waters with the prevailing SSC during the dry season. However, total results are not sensitive enough to reveal an impact of the Yangtze River dams (especially, the TGD) on the total turbid area in YRE and ACA. This fact may be explained by the relatively small area of the YRE relative to whole area under consideration.

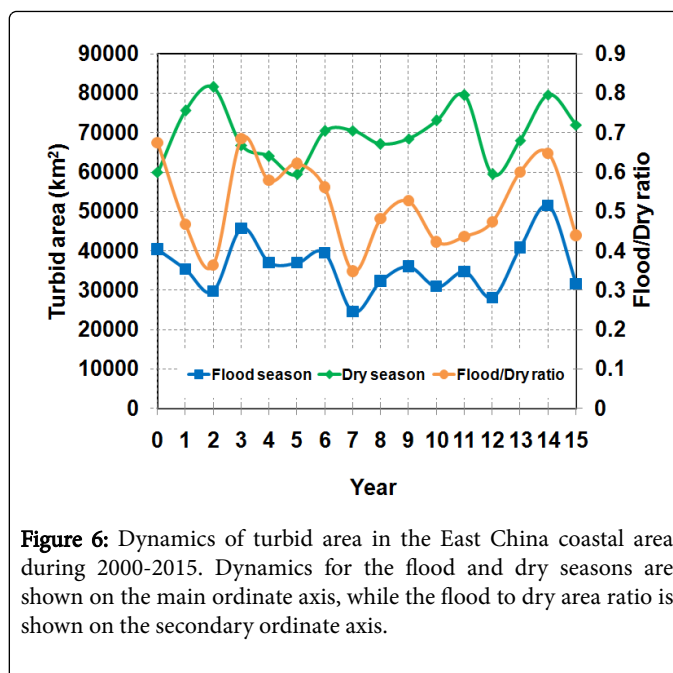


Figure 6: Dynamics of turbid area in the East China coastal area during 2000-2015. Dynamics for the flood and dry seasons are shown on the main ordinate axis, while the flood to dry area ratio is shown on the secondary ordinate axis.

The similar analysis performed for separate regions shows that Subei Bank and Zhejiang coastal area are among the most dramatically variable regions. For example, during the wet seasons, the Subei Bank high turbid area (with $SSC > 80 \text{ gm}^{-3}$) has varied from 4600 km² in 2007 to 23600 km² in 2014, at an average area of 12300 km². The high turbid area for the same region, but during the dry season, is significantly larger, even though variations are less dramatic: from 24600 km² in 2005 up to 42000 km² in 2002, with the average area of 32300 km².

Another important finding is decreasing SSC with increasing distance from the coastal line during whole year and along the whole coastal line. However, huge tongue-shaped "clouds" of more turbid waters (plumes) extend from the coast to the open parts of the ECS between approximately 31.5°N and 33°N, sometimes achieving a longitude of 126°E (see Figure 7 as example). These plumes are more expressed during dry seasons that was noted also by Ref. [26,36-38,43-46], but there is no consensus on the mechanisms of this phenomenon. For example, Shi and Wang [26] found that the main reason of formation of the plume is the strong mixing in the water column that, in turn, explained by shallow water depths, strong surface cooling, and high wind conditions. However, Chen et al. [45] suggested other reasons for plume formation in the Bohai, Yellow, and East China Seas, namely, river discharge, tidal and oceanic currents. Thus, this phenomenon obviously deserves further research.

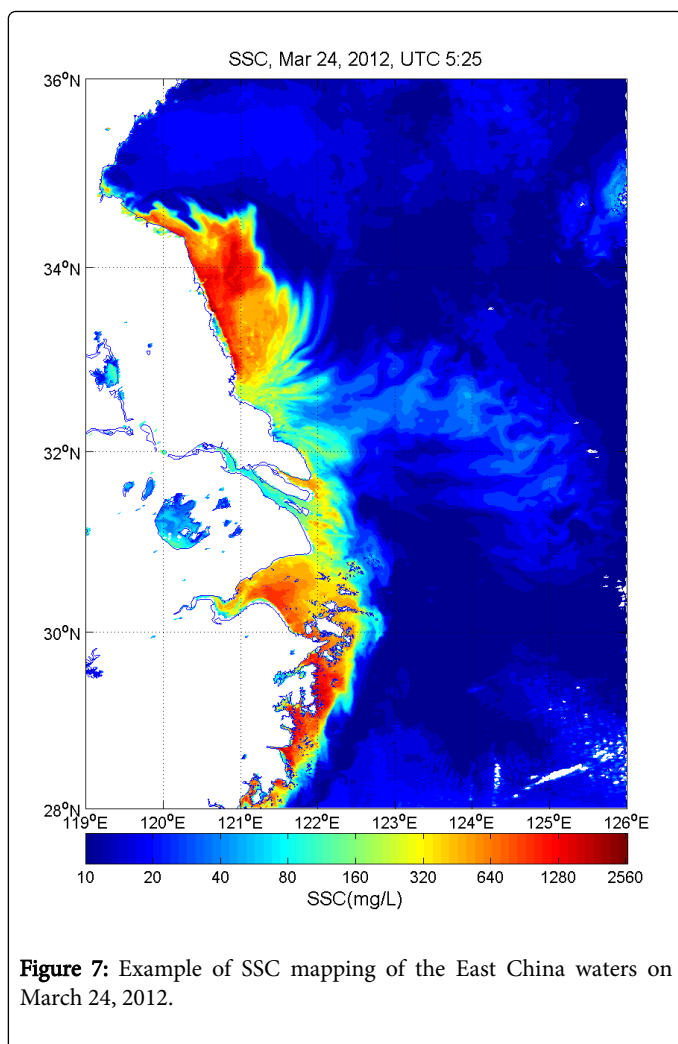


Figure 7: Example of SSC mapping of the East China waters on March 24, 2012.

Conclusions

Three separate algorithms: 1) Modified NIR-SWIR atmospheric correction, 2) Suspended sediment concentration (SSC), and 3) Diffuse attenuation coefficient at 490 nm, $K_d(490)$ were developed and used for mapping SSC and $K_d(490)$ for the East China natural waters. Based on these findings, we have presented satellite-based maps of SSC and $K_d(490)$ during 2000-2015 time period. Three main issues have been addressed in the study:

- Impact of dry and wet seasons on the water quality [expressed via SSC, $K_d(490)$, and high turbid area] in the region;
- Impact of the Three Gorges Dam (TGD) power station on the water quality;
- Plume formation in the region.

We have found, in particular, that Hangzhou Bay, Yangtze River Estuary and Subei Bank are the most turbid areas in the region (and, probably, in the world). Especially high levels of SSC and high turbid areas were observed during dry seasons. Concerning wet seasons, turbidity in the South Branch of YRE was significantly reduced after the TGD completion. Huge plumes of more turbid waters extending toward East China Sea were also observed on satellite-based images.

Acknowledgments

The research leading to these results has received funding from the National Science Foundation of China (grants number 41271375 and 41371346). We would like also to express our gratitude to the two anonymous reviewers for their constructive and helpful feedback on earlier drafts of this paper.

References

1. Morel A, Prieur L (1977) Analysis of variations in ocean color. *Limnol Oceanogr* 22: 709-722.
2. Gordon HR, Evans RH (1994) Coastal zone color scanner "system calibration": A retrospective examination. *J Geophys Res* 99: 7293-7307.
3. Mobley CD, Stramski D, Bissett WP, Boss E (2004) Optical modeling of ocean water - Is the Case 1 - Case 2 classification still useful? *Oceanogr* 17: 60-67.
4. Kondratyev KY, Pozdnyakov DV, Pettersson LH (1998) Water quality remote sensing in the visible spectrum. *Int J Remote Sens* 19: 957-979.
5. Boss E, Pegau WS, Gardner WD, Zaneveld JRV, Barnard AH, et al. (2001) Spectral particulate attenuation and particle size distribution in the bottom boundary layer of a continental shelf. *J Geophys Res* 106: 9509-9516.
6. Doxaran D, Froidefond JM, Castaing P (2002) A reflectance band ratio used to estimate suspended matter concentrations in sediment-dominated coastal waters. *Int J Remote Sens* 23: 5079-5085.
7. Pozdnyakov DV, Kondratyev KY, Bukata RP, Jerome JH (1998) Numerical modelling of natural water colour: Implications for remote sensing and limnological studies. *Int J Remote Sens* 19: 1913-1932.
8. Ahn YH, Moon JE, Gallegos S (2001) Development of suspended particulate matter algorithms for ocean color remote sensing. *Korean J Remote Sens* 17: 285-295.
9. Ouillon S, Douillet P, Petrenko A, Neveux J, Dupouy C, et al. (2008) Optical algorithms at satellite wavelengths for total suspended matter in tropical coastal waters. *Sensors* 8: 4165-4185.
10. Ouillon S, Douillet P, Andrefouet S (2004) Coupling satellite data with *in situ* measurements and numerical modeling to study fine suspended-sediment transport: a study for the lagoon of New Caledonia. *Coral Reefs* 23: 109-122.
11. Kumari VR, Rao IM (2010) Suspended sediment dynamics in Krishna estuary, east coast of India. *Indian J Mar Sci* 39: 248-256.
12. Wang Y, Shen J, He Q (2010) A numerical model study of the transport timescale and change of estuarine circulation due to waterway constructions in the Changjiang Estuary, China. *J Mar Syst* 82: 154-170.
13. Jerlov NG (1976) *Marine Optics*. Elsevier Scientific, New York, USA, pp: 1-230.
14. Prieur L, Sathyendranath S (1981) An optical classification of coastal and oceanic waters based on the specific spectral absorption curves of phytoplankton pigments, dissolved organic matter, and other particulate materials. *Limnol Oceanogr* 26: 671-689.
15. Baker KS, Smith RC (1982) Bio-optical classification and model of natural waters.2. *Limnol Oceanogr* 27: 500-509.
16. Morel A, Berthon JF (1989) Surface pigments, algal biomass profiles, and potential production of the euphotic layer: Relationships reinvestigated in view of remote-sensing applications. *Limnol Oceanogr* 34: 1545-1562.
17. Kaczmarek S, Woźniak B (1995) The application of the optical classification of waters in the Baltic Sea investigation (Case 2 waters). *Oceanologia* 37: 285-297.
18. Pelevin VN, Rutkovskaya VA (1997) On the optical classification of the ocean waters by the spectral solar light attenuation. *Oceanology* 17: 15-21.
19. Sokoletsky L, Shen F (2013) Turbidity classification of Chinese natural waters. Poster in: Asian Workshop on Ocean Color (AWOC) 2013, Tainan, Taiwan.

20. Sokoletsky LG, Shen F (2014) Optical closure for remote-sensing reflectance based on accurate radiative transfer approximations: the case of the Changjiang (Yangtze) River Estuary and its adjacent coastal area, China. *Int J Remote Sens* 35: 4193-4224.
21. Platt T, Sathyendranath S (1988) Oceanic primary production: Estimation by remote sensing at local and regional scales. *Science* 241: 1613-1620.
22. Antoine D, Morel A (1996) Oceanic primary production: I. Adaptation of a spectral light-photosynthesis model in view of application to satellite chlorophyll observations. *Global Biogeochem Cycles* 10: 43-55.
23. Capuzzo E (2011) Measuring and modelling the primary production of a Sea Lough in Northern Ireland. PhD thesis, Edinburgh Napier University, Edinburgh, UK, pp: 1-319.
24. Mueller JL (2000) SeaWiFS algorithm for the diffuse attenuation coefficient, K (490), using water-leaving radiances at 490 and 555 nm. In: *SeaWiFS Postlaunch Calibration and Validation Analyses, Part 3*, NASA Goddard Space Flight Cent, Greenbelt, USA, 11: 24-27.
25. Wang M, Son SH, Harding LW Jr (2009) Retrieval of diffuse attenuation coefficient in the Chesapeake Bay and turbid ocean regions for satellite ocean color applications. *J Geophys Res* vol: 114.
26. Shi W, Wang M (2010) Satellite observations of the seasonal sediment plume in central East China Sea. *J Mar Syst* 82: 280-285.
27. Chen S (2001) Seasonal, neap-spring variation of sediment concentration in the joint area between Yangtze Estuary and Hangzhou Bay. *Sci China* 44: 57-62.
28. Chen SL, Zhang GA, Yang SL, Shi JZ (2006) Temporal variations of fine suspended sediment concentration in the Changjiang River Estuary and adjacent coastal waters, China. *J Hydrol* 331: 137-145.
29. Wang JJ, Lu XX, Zhou Y (2007) Retrieval of suspended sediment concentrations in the turbid waters of the Upper Yangtze River using Landsat ETM+. *Chin Sci Bul* 52: 273-280.
30. Jiang X, Tang J, Zhang M, Ma R, Ding J (2009) Application of MODIS data in monitoring suspended sediment of Taihu Lake, China. *Chin J Oceanol Limnol* 27: 614-620.
31. Shen F, Verhoef W, Zhou Y, Salama MS, Liu X (2010) Satellite estimates of wide-range suspended sediment concentrations in Changjiang (Yangtze) estuary using MERIS data. *Est Coasts* 33: 1420-1429.
32. Wang JJ, Lu XX (2010) Estimation of suspended sediment concentrations using Terra MODIS: An example from the Lower Yangtze River, China. *Sc Total Envir* 408: 1131-1138.
33. Zhang M, Tang J, Dong Q, Song Q, Ding J (2010) Retrieval of total suspended concentration in the Yellow and East China Seas from MODIS imagery. *Remote Sens Envir* 114: 392-403.
34. Wang M, Shi W, Tang J (2011) Water property monitoring and assessment for China's inland Lake Taihu from MODIS-Aqua measurements. *Rem Sensing Envir* 115: 841-854.
35. Li P, Yang SL, Milliman JD, Xu KH, Qin WH, et al. (2012) Spatial, temporal, and human-induced variations in suspended sediment concentration in the surface waters of the Yangtze Estuary and adjacent coastal waters. *Est Coasts* 35: 1316-1327.
36. Shi W, Wang M (2012) Satellite views of the Bohai Sea, Yellow Sea, and East China Sea. *Progress Oceanogr* 104: 30-45.
37. Wang M, Shi W, Jiang L (2012) Atmospheric correction using near-infrared bands for satellite ocean color data processing in the turbid western Pacific region. *Opt Express* 20: 741-753.
38. Mao Z, Chen J, Pan D, Tao B, Zhu Q (2012) A regional remote sensing algorithm for total suspended matter in the East China Sea. *Rem Sensing Envir* 124: 819-831.
39. He X, Bai Y, Pan D, Huang N, Dong X, et al. (2013) Using geostationary satellite ocean color data to map the diurnal dynamics of suspended particulate matter in coastal waters. *Rem Sensing Envir* 133: 225-239.
40. Jiang X, Lu B, He Y (2013) Response of the turbidity maximum zone to fluctuations in sediment discharge from river to estuary in the Changjiang Estuary (China). *Est Coast Shelf Sci* 131: 24-30.
41. Qiu Zh, Wu T, Su Y (2013) Retrieval of diffuse attenuation coefficient in the China seas from surface reflectance. *Opt Express* 21: 15287-15297.
42. Shen F, Zhou Y, Li J, He Q, Verhoef W (2013) Remotely sensed variability of the suspended sediment concentration and its response to decreased river discharge in the Yangtze estuary and adjacent coast. *Cont Shelf Res* 69: 52-61.
43. Shen F, Zhou Y, Peng X, Chen Y (2014) Satellite multi-sensor mapping of suspended particulate matter in turbid estuarine and coastal ocean, China. *Int J Remote Sens* 35: 4173-4192.
44. Sokoletsky L, Yang X, Shen F (2014) MODIS-based retrieval of suspended sediment concentration and diffuse attenuation coefficient in Chinese estuarine and coastal waters. *Proc SPIE Asia Pacific Remote Sensing*, 9261: 926119-1-926119-25
45. Chen J, Quan W, Cui T, Song Q (2015) Estimation of total suspended matter concentration from MODIS data using a neural network model in the China eastern coastal zone. *Est Coast Shelf Sci* 155: 104-113.
46. Yang X, Sokoletsky L, Wei X, Shen F (2016) Suspended sediment concentration mapping based on the MODIS satellite imagery in the East China inland, estuarine, and coastal waters. *Chin J Oceanol Limnol* 35: 39-60.
47. Mao C, Chen J, Yuan X, Yang Z, Balsam W, et al. (2010) Seasonal variation in the mineralogy of the suspended particulate matter of the lower Changjiang River at Nanjing, China. *Clays Clay Miner* 58: 691-706.
48. Yang SL, Milliman JD, Li P, Xu K (2011) 50,000 dams later: Erosion of the Yangtze River and its delta. *Glob Planet Change* 75: 14-20.
49. Gordon HR (1978) Removal of atmospheric effects from satellite imagery of the oceans. *Appl Opt* 17: 1631-1636.
50. Gordon HR, Clark DK (1981) Clear water radiances for atmospheric correction of coastal zone color scanner imagery. *Appl Opt* 20: 4175-4180.
51. Gordon HR, Castaño DJ (1987) Coastal Zone Color Scanner atmospheric correction algorithm: multiple scattering effects. *Appl Opt* 26: 2111-2122.
52. Wang M, Gordon HR (1994) Radiance reflected from the ocean-atmosphere system: synthesis from individual components of the aerosols size distribution. *Appl Opt* 33: 7088-7095.
53. Gordon HR (1997) Atmospheric correction of ocean color imagery in the Earth Observing System era. *J Geophys Res* 102: 17081-17106.
54. Wang M, Shi W (2005) Estimation of ocean contribution at the MODIS near-infrared wavelengths along the east coast of the U.S.: Two case studies. *Geophys Res Lett* 32: 13606-13610.
55. Kaufman YJ, Wald AE, Remer LA, Gao BC, Li RR, et al. (1997) The MODIS 2.1- μm channel — Correlation with visible reflectance for use in remote sensing of aerosol. *IEEE Trans Geosci Remote Sens* 35: 1286-1298.
56. Remer LA, Kaufman YJ, Tanré D, Mattoo S, Chu DA, et al. (2005) The MODIS aerosol algorithm, products, and validation. *J Atmos Sci* 62: 947-973.
57. Tanré D, Kaufman YJ, Herman M, Mattoo S (1997) Remote sensing of aerosol properties over oceans using the MODIS/EOS spectral radiances. *J Geophys Res* 102: 16971-16988.
58. Levy RC, Remer LA, Tanré D, Kaufman YJ, Ichoku C, et al. (2003) Evaluation of the Moderate-Resolution Imaging Spectroradiometer (MODIS) retrievals of dust aerosol over the ocean during PRIDE. *J Geophys Res* 108: 8594.
59. Shi W, Wang M (2007) Detection of turbid waters and absorbing aerosols for the MODIS ocean color data processing. *Remote Sens Environ* 110: 149-161.
60. Wang M, Shi W (2007) The NIR-SWIR combined atmospheric correction approach for MODIS ocean color data processing. *Optics Express* 15: 15722-15733.
61. Tanré D, Deschamps PY, Devaux C, Herman M (1988) Estimation of Saharan aerosol optical thickness from blurring effects in Thematic Mapper data. *J Geophys Res* 93: 15955-15964.
62. Holben BN, Kaufman YJ, Setzer AW, Tanré DD, Ward DE (1991) Optical properties of aerosol emissions from biomass burning in the tropics, BASE-A. In *Global Biomass Burning: Atmospheric, Climate and Biospheric Implications*. MIT Press, Cambridge, MA, USA, pp: 403-411.

-
63. Dubovik O, Holben B, Eck TF, Smirnov A, Kaufman YJ, et al. (2002) Variability of absorption and optical properties of key aerosol types observed in worldwide locations. *J Atm Sci* 59: 590-608.
 64. Sokoletsky L, Shen F, Yang X, Wei X (2016) Evaluation of empirical and semi-analytical spectral reflectance models for surface suspended sediment concentration in the highly variable estuarine and coastal waters of East China. *IEEE J Sel Topics Appl Earth Observ Remote Sens* 9: 5182-5192.
 65. Vermote EF, Vermeulen A (1999) Atmospheric Correction Algorithm: Spectral Reflectances (MOD09). NASA contract NAS5-96062, Univ Maryland, College Park, MD, USA, pp: 1-107.
 66. Vermote EF, Roger JC, Ray JP (2015) MODIS Surface Reflectance User's Guide. Version 1.4, pp: 1-35.
 67. Gordon HR, Voss KJ (2004) MODIS Normalized Water-leaving Radiance Algorithm Theoretical Basis Document (MODIS 18). Version 5, Univ Miami, Coral Gables, FL, USA, pp: 1-125.
 68. Ruddick KG, Cauwer VD, Park YJ, Moore G (2006) Seaborne measurements of near infrared water-leaving reflectance: The similarity spectrum for turbid waters. *Limnol Oceanogr* 51: 1167-1179.
 69. Gordon HR, Brown OB (1974) Influence of bottom depth and albedo on the diffuse reflectance of a flat homogeneous ocean. *Appl Opt* 13: 2153-2159.
 70. Gordon HR, Brown OB, Jacobs MM (1975) Computed relationships between the inherent and apparent optical properties of a flat homogeneous ocean. *Appl Opt* 14: 417-427.
 71. Sokoletsky LG, Budak VP, Shen F, Kokhanovsky AA (2014) Comparative analysis of radiative transfer approaches for calculation of plane transmittance and diffuse attenuation coefficient of plane-parallel light scattering layers. *Appl Opt* 53: 459-468.
 72. Solonenko MG, Mobley CD (2015) Inherent optical properties of Jerlov water types. *Appl Opt* 54: 5392-5401.